Supporting Information

Yonghui Zhang[a,b], Fan Li[c,d], Tianyu Li[a], Mengqi Zhang[a,c], Zhizhang Yuan[a], Guangjin Hou[c], Jie Fu[b], Changkun Zhang[a*] and Xianfeng Li[a*]*

[a]Division of Energy Storage, Dalian National Laboratory for Clean Energy, Dalian Institute of Chemical Physics, Chinese Academy of Sciences, 457 Zhongshan Road, Dalian 116023, China.
[b]College of Environmental and Chemical Engineering, Dalian Jiaotong University, 794 Huanghe Road, Dalian, 116028, China.
[c]University of Chinese Academy of Sciences, Beijing 100049, China.
[d]State Key Laboratory of Catalysis, Dalian National Laboratory for Clean Energy (DNL), Dalian Institute of Chemical Physics, Chinese Academy of Sciences, Dalian, China.
*Corresponding author E-mails: fj@djtu.edu.cn, zhangchk17@dicp.ac.cn, and lixianfeng@dicp.ac.cn

Experimental Section

Materials. Methylene Blue (MB, high purity), 98% H_2SO_4, and glacial acetic acid (AA) were from Innochem. PBI-AB25 membrane[1] were home-made.

Electrochemical measurements. RDE and RRDE voltammetry were conducted using a Gamry Multichannel System installation (Gamry Interface 1000) and a E7R9 RRDE rotating ring disk electrode. CV used the glassy carbon electrode as working electrode (3 mm diameter). Both CV, RDE and RRDE test used Ag/AgCl as reference electrode, platinum wire as counter electrode and glassy carbon as working electrode. For RRDE experiments, current was measured in the potential range of 0-0.6 V versus Ag/AgCl at 10 mV s^{-1}. The rotation rates were 200, 400, 600, 800, 1000, 1200,1400, 1600, 1800, 2000, 2500 rpm. For RDE experiments, current was measured in the potential range of 0-0.6 V versus Ag/AgCl at 10 mV s^{-1}. The rotation rates were 400, 625, 900, 1225, 1600, 2025, 2500 rpm. The diffusion coefficient (D_0) at different H_2SO_4 concentrations was calculated according to Levich equation: $i_{lim} = 0.62nFAD_0^{2/3}\omega^{1/2}v^{-1/6}C$, where i_{lim} is limiting current, n is the number of electrons transferred (n = 2 for MB), F is the Faraday constant (96485 C mol^{-1}), A is the surface area of the working electrode (0.2475 cm^2), C is molar concentration in 1 × 10^{-5} mol cm^{-3}, v is the kinetic viscosity in cm^2 s^{-1} and ω is the routing angular velocity in rad s^{-1}. The reaction rate constant (k_0) at different AA concentrations was calculated at each potential using the Koutecky-Levich equation:

$$\frac{1}{i} = \frac{1}{i_k} + \frac{1}{0.62nAFD_0^{\frac{2}{3}}\omega^{\frac{1}{2}}v^{-\frac{1}{6}}C}$$

The exchange current (i_0) can be obtained by fitting i_k to the Tafel plot at the overpotential of zero, from which the k_0 was determined according to Butler-Volmer equation: $i_0 = nFACk_0$.

Dynamic viscosity ($\mu = v \times \rho$) in mPa·s are 1.86, 2.67, 3.35, 4.45 and 6.28 mPa·s for 0, 0.2, 0.3, 0.4 and 0.6 volume ratio of acetic acid in 3 M H_2SO_4 solution.

Battery performance. 10 units FB stack were assembled with an area of 1000 cm^2 commercial carbon felt with compression ratio of 3:2 and polybenzimidazole (PBI) of

AB-25 (scale bar, 25 μm) membrane[1]. The catholyte used the 20 L 0.1 M MB 5.25 M AA + 3 M H_2SO_4 and 0.5 M MB in 7 M AA + 3 M H_2SO_4 electrolytes, respectively. The single cells used the same ratio. The anolyte is 30 L 1.5 M V (II) (in 3 M H_2SO_4). Tanks volumes on both sides are 60 L and they are all direct exposure to air without nitrogen gas protection. The polarization curve and power densities of the stack were measured at room temperature at 100% SOC. The current density ranges from 0 mA cm^{-2} to 210 mA cm^{-2}, increasing by 5 mA cm^{-2} per second.

Pausing cycling test. 0.5 M V-MB cell was run with resting time after complete discharging for several times. The resting time are 12, 24 and 48 hours, respectively.

Characterizations.

Ex situ NMR. The 1H nuclear magnetic resonance (NMR) of different electrolytes were conducted on a 400 MHz NMR spectrometer (Bruker AV400).

In situ NMR. The in-situ NMR was measured by a 400MHz NMR spectrometer (Bruker AVANCE NEO 400M). 0.5 M MB and 1.5 M V (II) were used as anolyte as catholyte, respectively. At 90 mA (10 mA cm^{-2}) constant current, the battery first discharged and then charged, which corresponded to a complete cycle of MB from oxidation state to reduction state and then to oxidation state.

Ex-situ EPR. The electron paramagnetic resonance (EPR) spectra of electrolytes were conducted on a Bruker A200 EPR spectrometer.

LC-MS. Decomposition compounds of the MB electrolyte was detected by the liquid chromatography−mass spectroscopy (LC-MS).

Fourier Transform Infrared Spectroscopy (FT-IR) experiments were carried out on Nicolet iS50 (Thermo Fisher).

Theoretical calculation.

All calculations were performed using density functional theory (DFT) with Gaussian 16[2] package. Firstly, the B3LYP[3] hybrid functional at 6-31G(d) level of basis set including the atom-pairwise dispersion (DFT-D3) correction[4, 5] with Becke-Johnson (BJ) damping[6], was applied for geometry optimization. Then the optimized structures were checked by vibrational frequency analysis[7] at the same calculation level to ensure the they were on the local minima of potential energy surface. The solvation energy

was obtained by subtracting the energy of vacuum from the energy of liquid phase. The energy of vacuum (E_{vacuum}) was calculated at M05-2X[8]/6-31G(d) level with DFT-D3 correction. The energy of liquid phase (E_{SMD}) was calculated at M05-2X/6-31G(d) with implicit universal water solvation model based on solute electron density (SMD)[9] and with DFT-D3 correction. A single-point calculation (E_{high}) was carried out at B3LYP/def2-TZVP[10] also including the DFT-D3(BJ) correction. The Gibbs free energy (G) was calculated,

$$G=E_{high}+(E_{SMD}-E_{vacuum}+1.89*4.184 \text{ kj/mol})+G_{correction}$$

where $G_{correction}$ was the frequency correction which was calculated by the Shermo 2.1.2[11] package. The spin density was analyzed by Multiwfn[12] package and drawn by VMD[13] software. The localized orbital locator (LOL) of the π electron was analyzed and drawn by Multiwfn package.

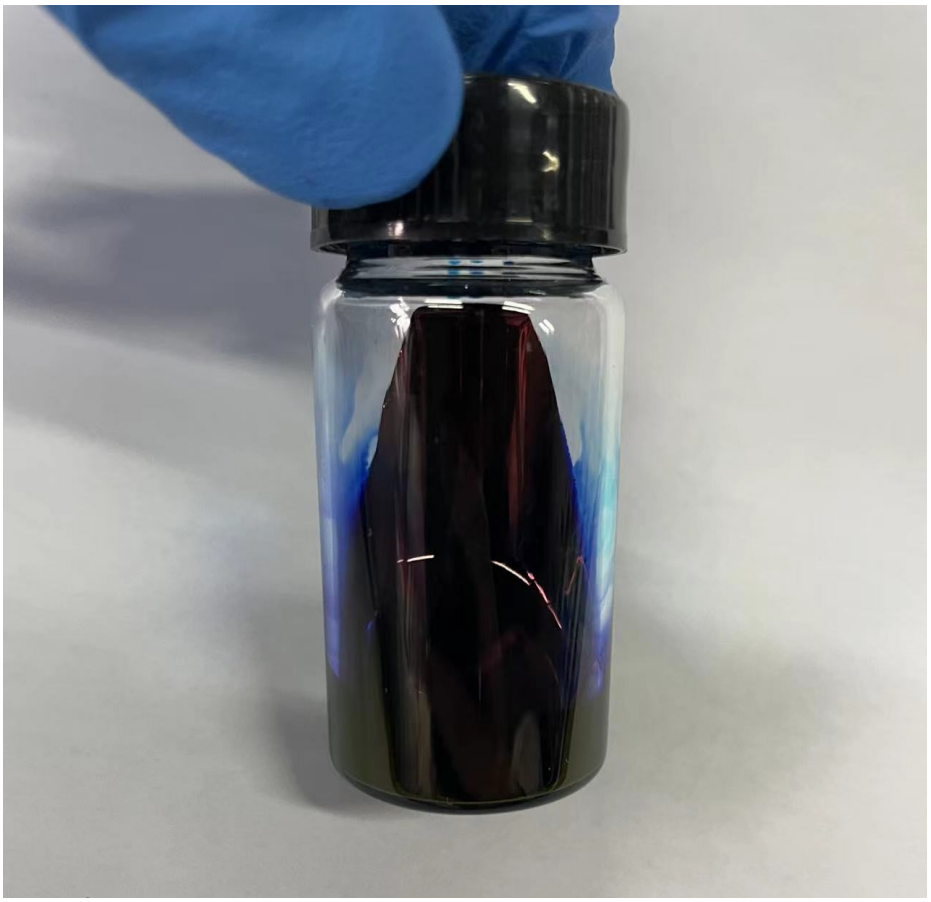

Fig. S1 The photo on the left is 1MB-4AA eutectic electrolyte

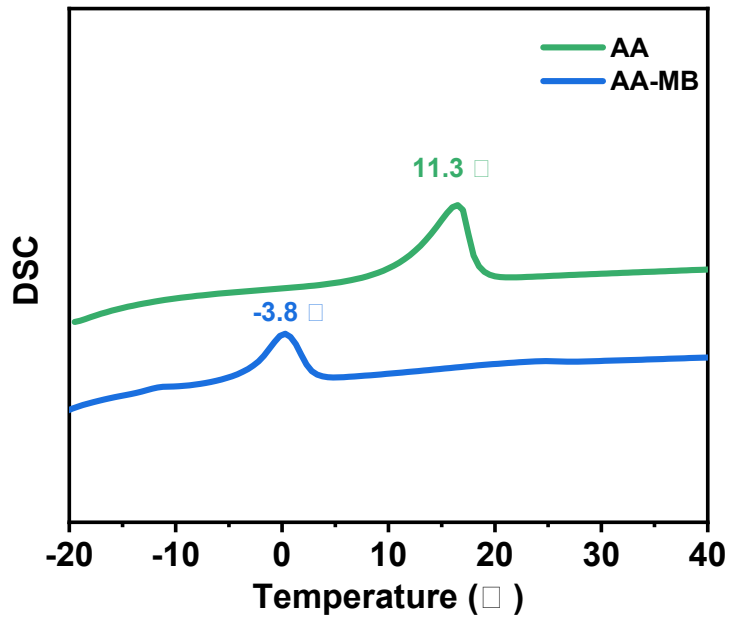

Fig. S2 DSC curves of pure AA and 1MB-4AA eutectic electrolyte

NMR spectra analysis (Fig. 1) revealed that the H signal *k* assigned to the methyl group of AA in the 1MB-4AA electrolyte shifted from 2.67 ppm to 1.93 ppm, when compared with the purity AA. While the 12.3 ppm assigned to the OH group disappeared due to the proton exchange between MB and AA molecule, which has also been observed in the AA-H_2O solution. Meanwhile, all the H signals of MB in 1MB-4AA eutectic electrolyte shifted to upfield when compared with MB in D_2O, suggesting the strong interaction between MB and AA molecules.

It can be found from DSC curves that the freezing point (T_c) of 1MB-4AA eutectic electrolyte was significantly reduced from 11.3℃ (the purity AA) to -3.8℃, indicating a strong interaction between AA and MB (Fig. 1b), corresponding to the NMR shifting.

Fig. S3 The photos of the two liquids at 0^{o}C.

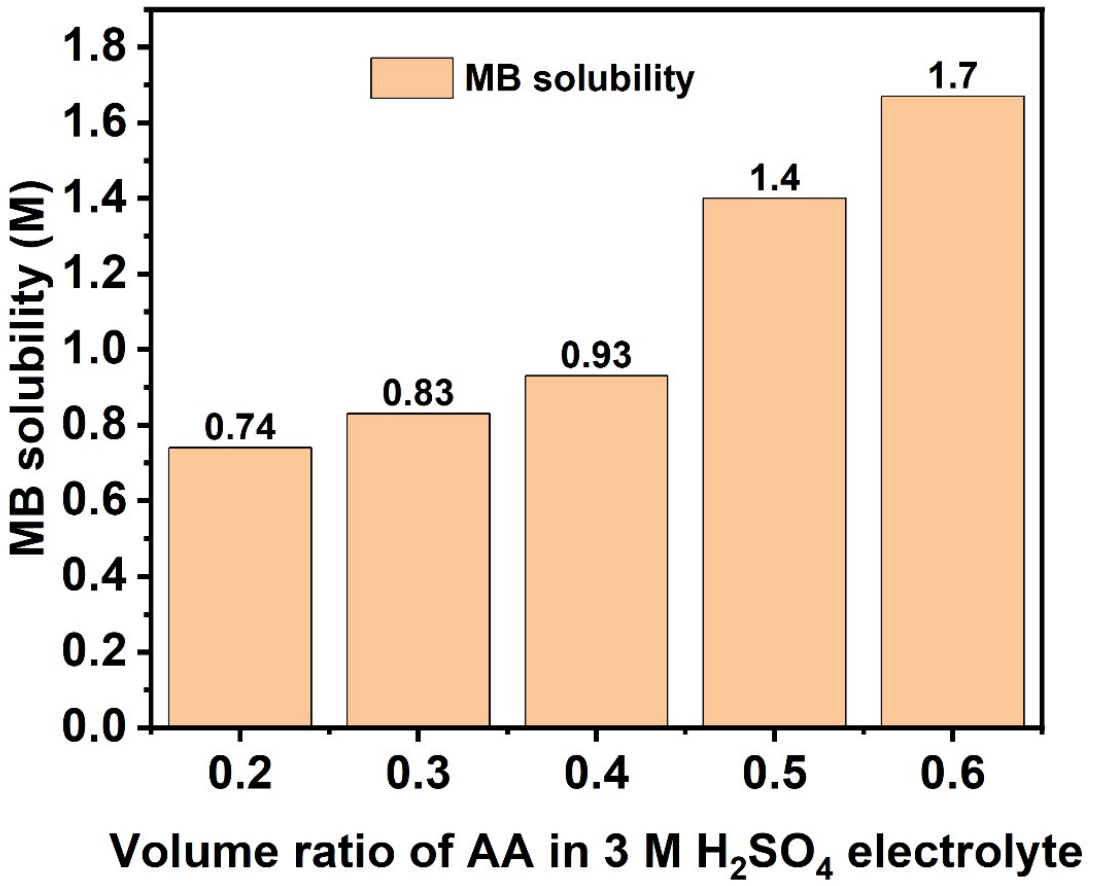

Fig.S4 Solubilities of MB molecules in different volume ratios of AA and 3 M H_2SO_4 electrolyte.

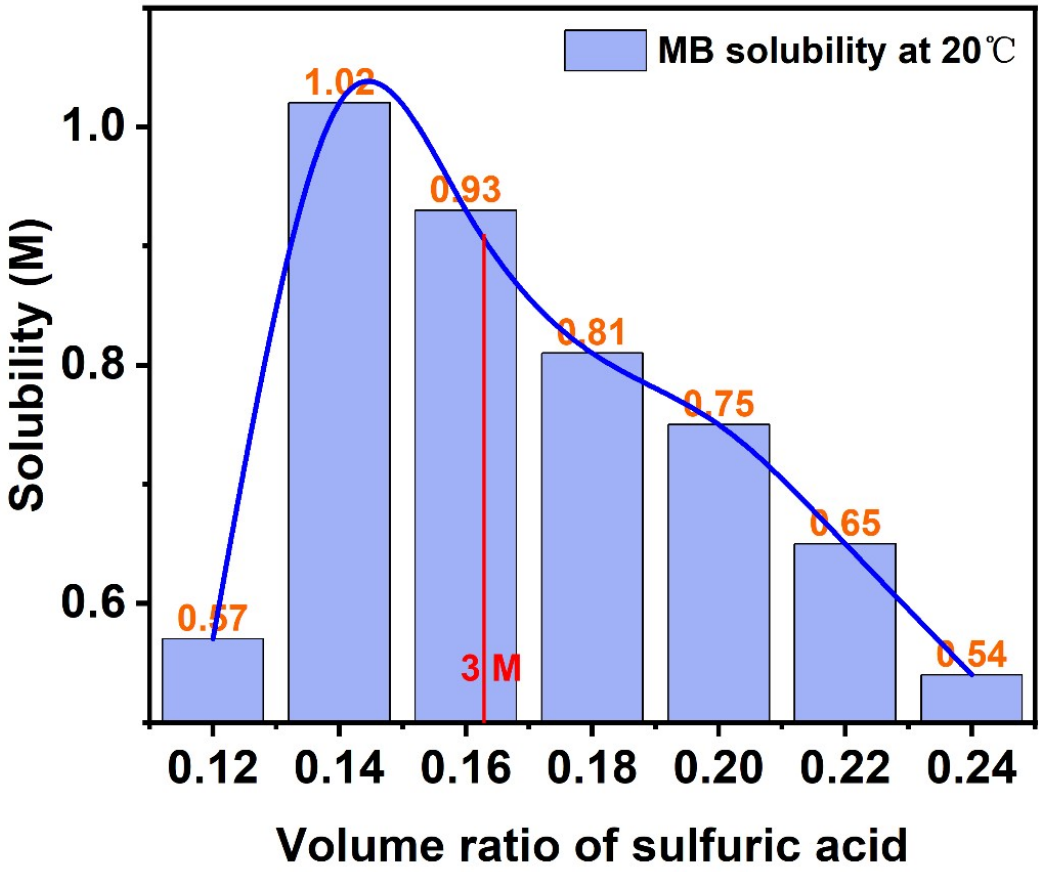

Fig. S5 Solubilities of MB molecules in 7 M AA and different sulfuric acid concentrations electrolytes.

With the presence of 3 M H_2SO_4, the concentration of MB can be 1.7 M which is nearly 2.4 times more than the electrolyte without H_2SO_4 at the AA-H_2O volume ratio of 0.6. However, there is optimal range for H_2SO_4 content, and the MB solubility reaches to the maximum at the H_2SO_4 concentration of around 2.6 M in 7 M AA electrolyte.

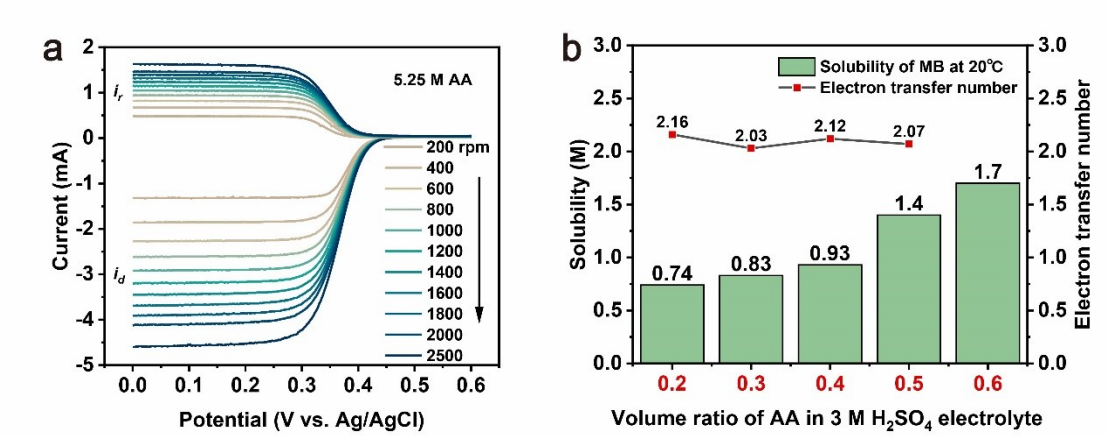

Fig. S6 (a) RRDE curves of 5.25 M AA electrolyte. (b) Solubility and electron transfer number of MB electrolytes with different AA contents.

Electron transfer number:

$$n = 4 \times \frac{|i_d|}{|i_d| + \frac{i_r}{N_c}} \quad (1)$$

Theoretical collection rate:

$$N = 1 - F\left(\frac{r_2^3 - r_1^3}{r_3^3 - r_2^3}\right) + \left(\frac{r_3^3 - r_2^3}{r_1^3}\right)^{\frac{2}{3}}\left[1 - F\left(\left(\frac{r_2}{r_1}\right)^3 - 1\right)\right] - \left(\frac{r_3}{r_1}\right)^2\left\{1 - F\left[\left(\frac{r_2^3 - r_1^3}{r_3^3 - r_2^3}\right)\left(\frac{r_3}{r_1}\right)^3\right]\right\} \quad (2)$$

Experimental collection rate:

$$N_c = \frac{j_r}{j_d} \quad (3)$$

where j_d (mA cm^{-2}) is disk current density, j_r (mA cm^{-2}) is ring current density, and N_c is collection rate of ring current, respectively.

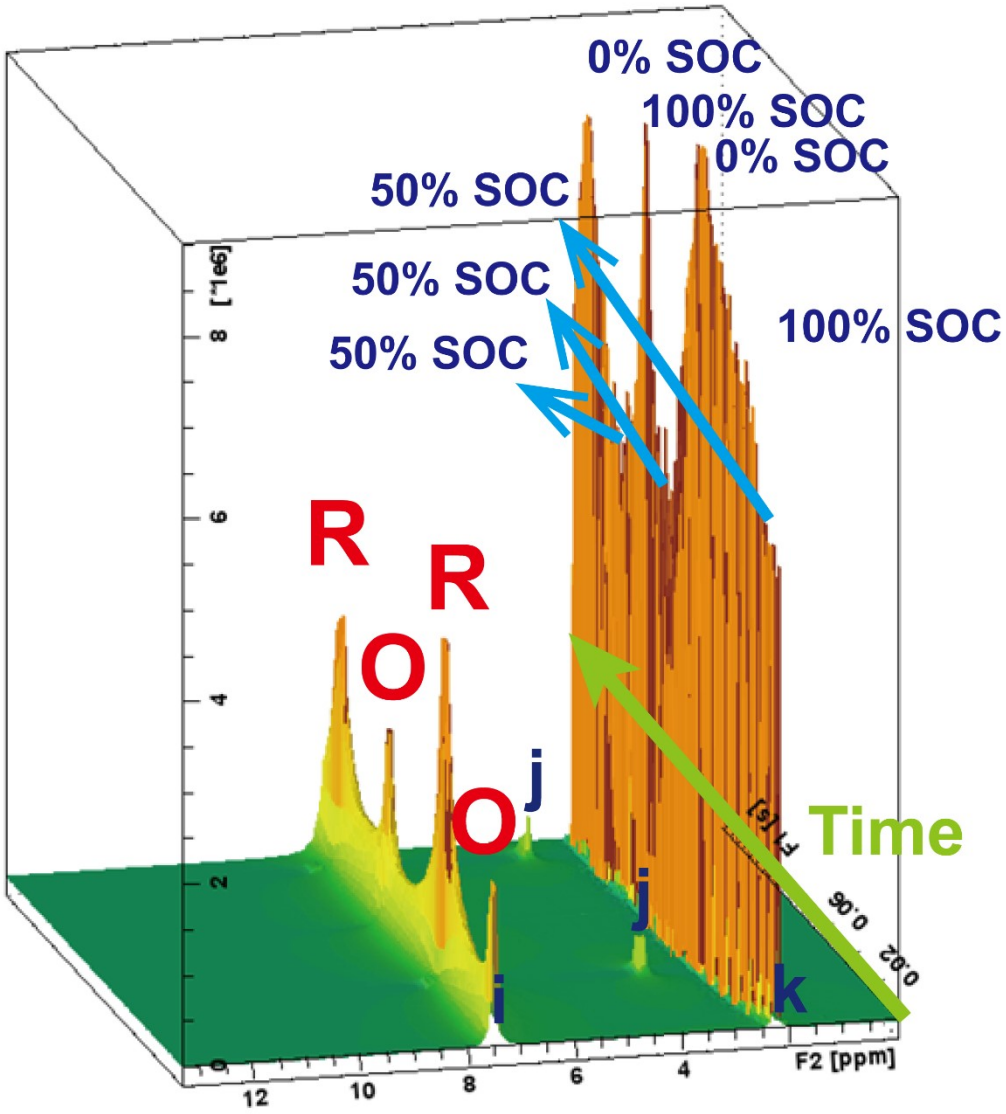

Fig. S7 the side view of ^{1}H_3D NMR spectrum from 0 to 13 ppm. O presents oxidation state of MB, that is MBH^{2+}. R presents reduction state, that is $HMBH^{2+}$.

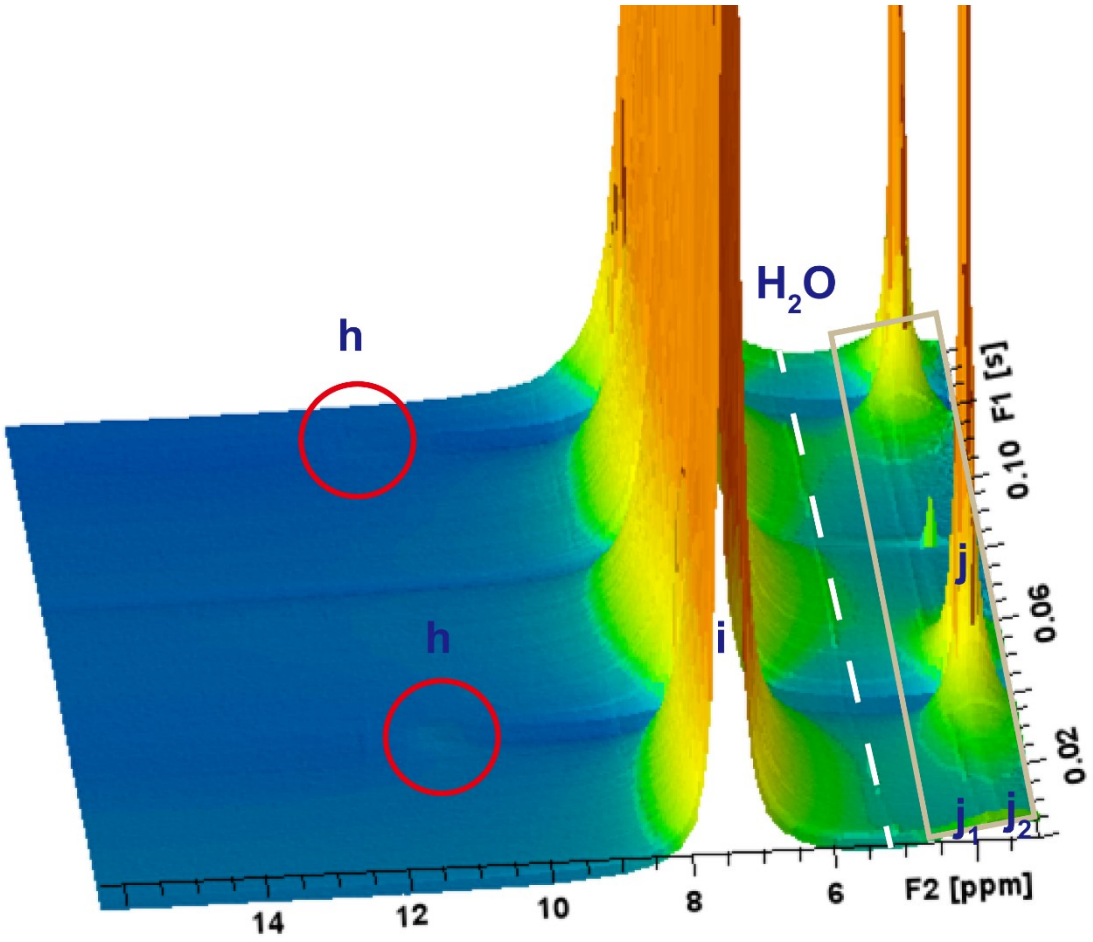

Fig. S8. A partial enlargement of ^{1}H_3D NMR spectrum from 3.5 to 16 ppm.

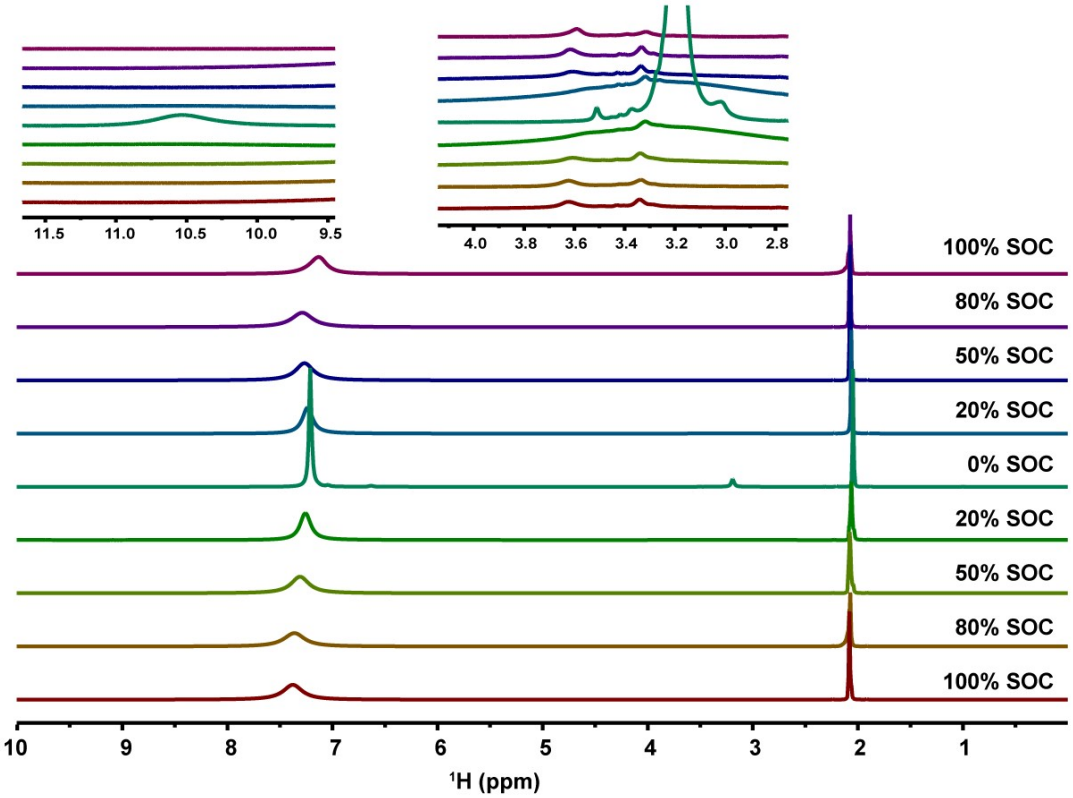

Fig. S9 Ex-situ NMR spectrum of 0.5 M MB at different SOC. The top left corner of the picture is the partial enlargement from 9.5 to 11.5 ppm. A partial enlargement from 2.8 to 4.0 ppm is shown directly above the image.

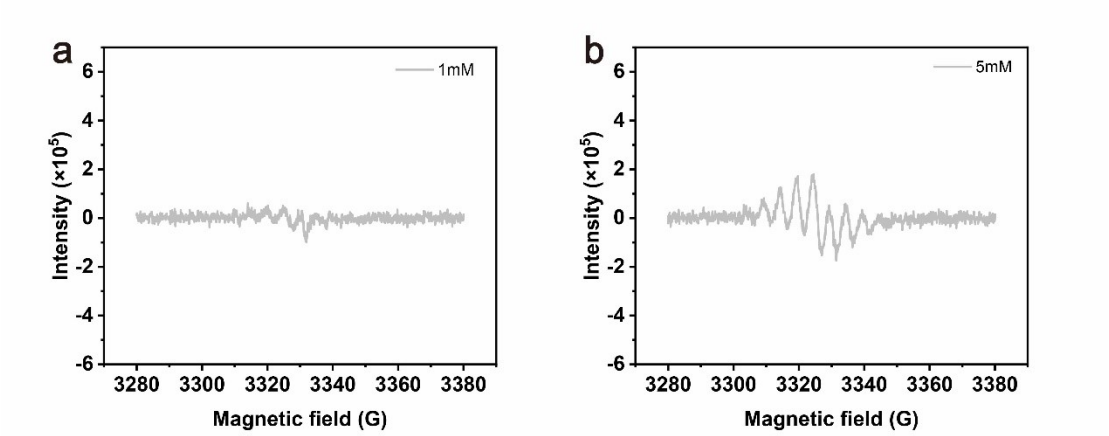

Fig. S10. EPR spectra of **a** 1 mM and **b** 5mM MB catholyte. The spectra were acquired at 50% SOC in a full cell with 0.1M MB/SWO during the last charge cycle, and were diluted to 1 mM and 5 mM, respectively.

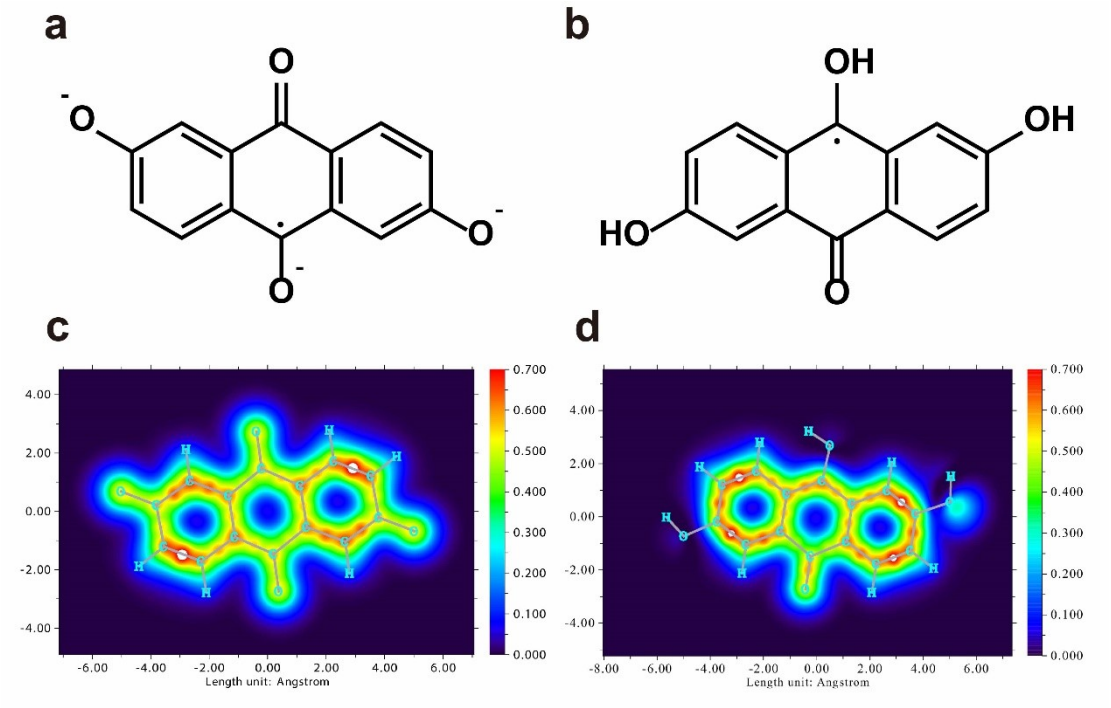

Fig. S11. The redox reaction of 2,6-dihydroxyanthraquinone (DHAQ) can form the radical anion, $DHAQ^{3-\bullet}$ under basic condition and $DHAQ^{\bullet}$ under acidic condition. **a** is structural formula of $DHAQ^{3-\bullet}$. **b** is structural formula of $DHAQ^{\bullet}$ **c** is the picture of $DHAQ^{3-\bullet}$ under basic condition through π-Localized orbital locator (LOL). **d** is the picture of $DHAQ^{\bullet}$ under acidic condition through π-Localized orbital locator (LOL).

Table. S1. The multicenter bond order distribution of radicals of $DHAQ^{3-\bullet}$, $DHAQ^{\bullet}$ and $MBH_2^{2+\bullet}$ are shown in the table. Left, Middle, Right represent benzene rings in different positions.

The multicenter bond order distribution	Left	Middle	Right
$DHAQ^{3-\bullet}$ under basic condition	0.0316	0.0111	0.0316
$DHAQ^{\bullet}$ under acidic condition	0.0426	0.0102	0.0419
$MBH_2^{2+\bullet}$	0.0363	0.0080	0.0495

Left Middle Right

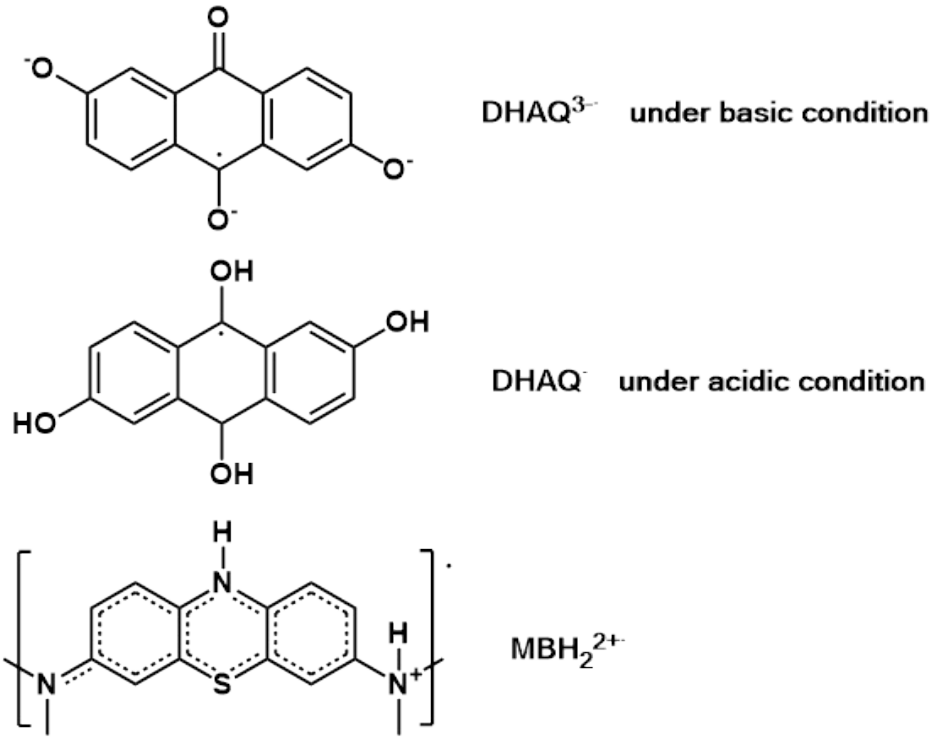

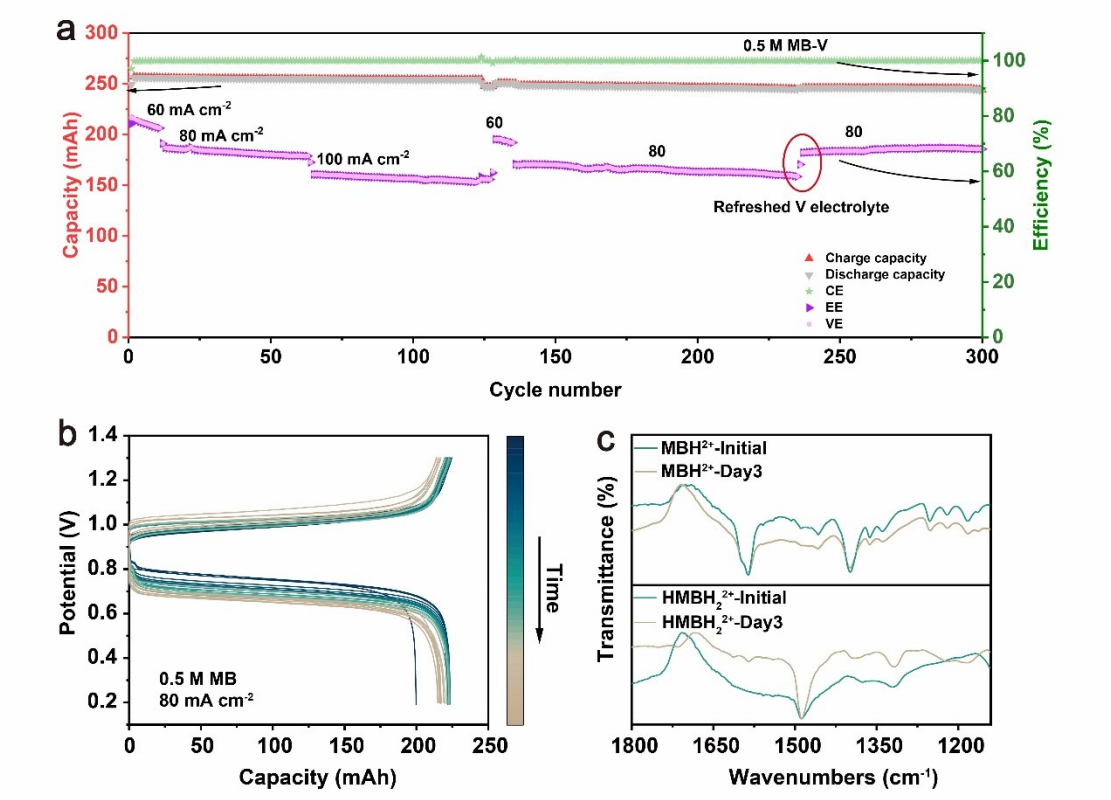

Fig. S12. a. The cycling performance of MB-V flow batteries at 60, 80 and 100 current densities. **b** Charge-discharge curves of first cycle after cycling pausing every time. **c** FTIR spectra for MBH^{2+} and $HMBH_2^{2+}$ and those after storing for 72 h.

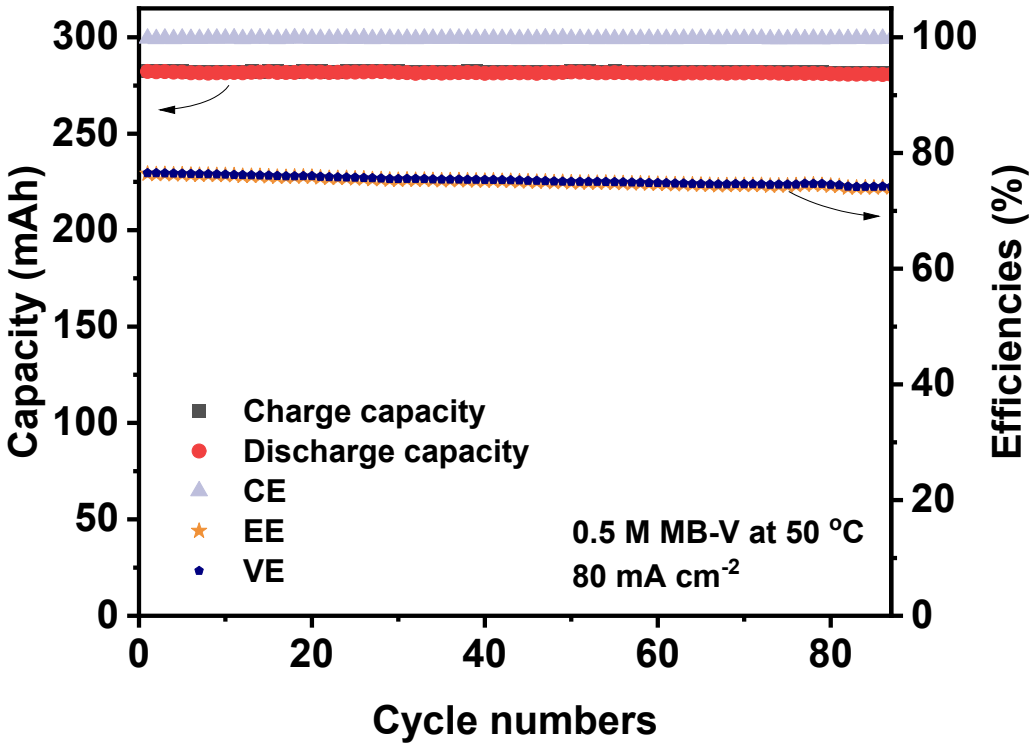

Fig. S13. 0.5 M MB-V Cell performance at 50 °C.

The operation of MB-V flow battery at 50 °C is stable with almost constant capacity retention rate.

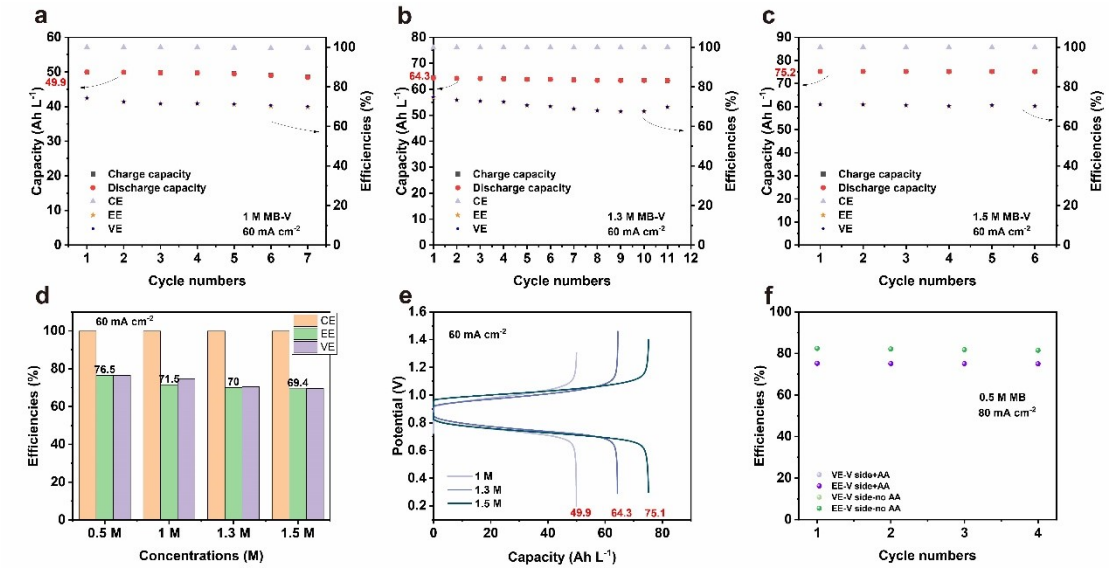

Fig. S14. Cells performance of high concentration of MB. **a-c** Cells cycle performance of 1 M, 1.3 M and 1.5 M MB, respectively. **d** Average cell efficiencies at different concentrations. **e** charge-discharge curves at different concentrations. **f** Effect of V cathode side with or without AA on battery energy efficiency (EE) and voltage efficiency (VE).

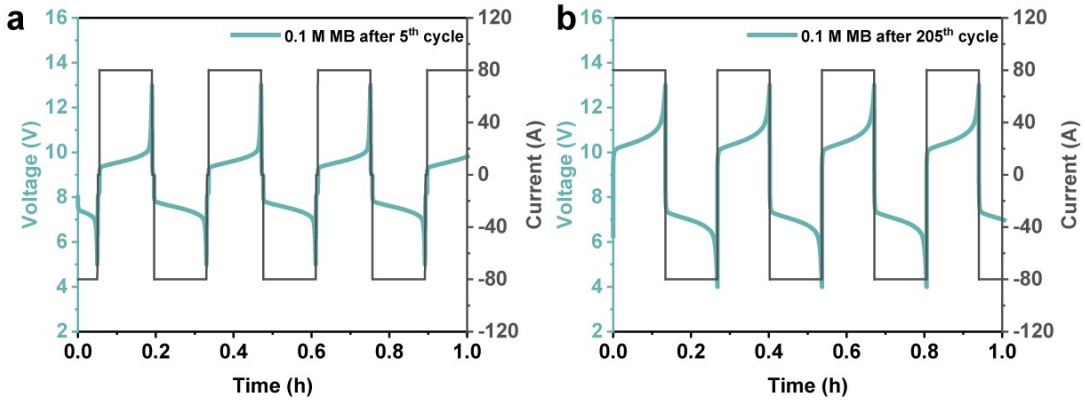

Fig. S15. Cell voltage-time and current-time curves of 0.1 M MB FBs stack at 80 mA cm^{-1}. **a** Galvanostatic cutoff voltages between 5 and 13 V before 205th cycle. **b** Galvanostatic cutoff voltages between 4 and 13 V cutoff after 205th cycle.

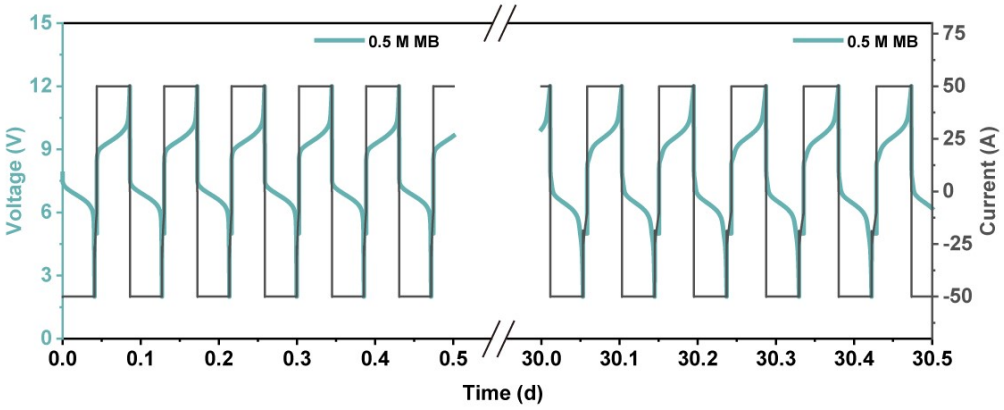

Fig. S16 Cell voltage-time and current-time curves of 0.5 M MB FBs stack for first and thirtieth days at 50 mA cm^{-1}.

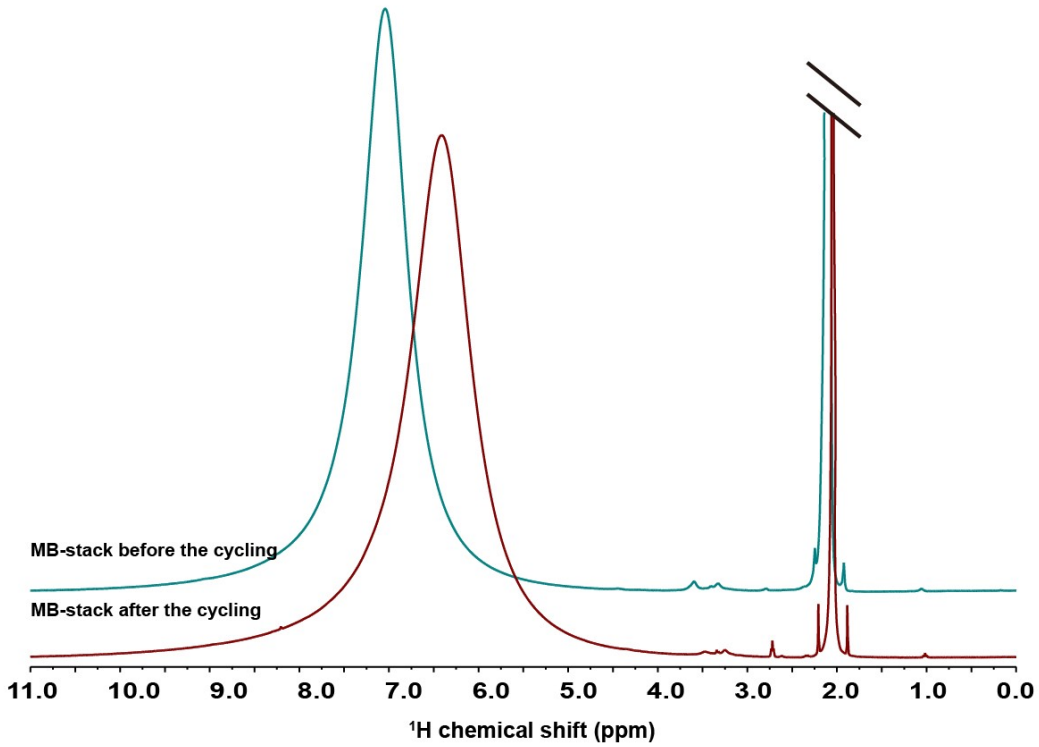

Fig. S17. NMR spectra of 0.1 M MB at 100% SOC before and at the end of the stack cycling.

Fig. S18. Photos of AB25 membranes before (left) and after (right) cycling.

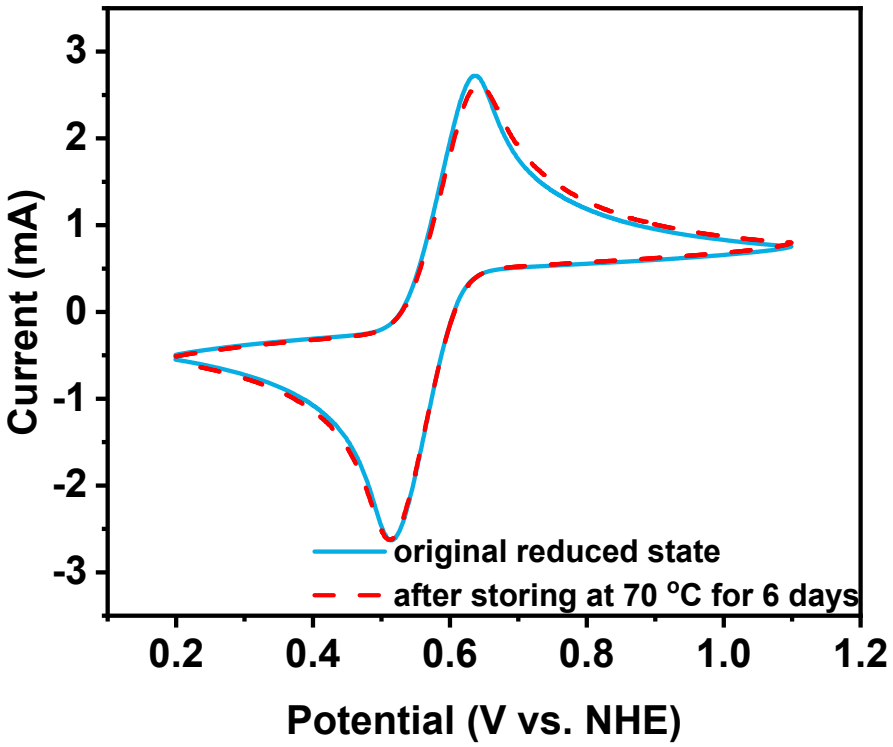

Fig. S19. CV curves of reduced state before and after storing at 70 °C for 6 days.

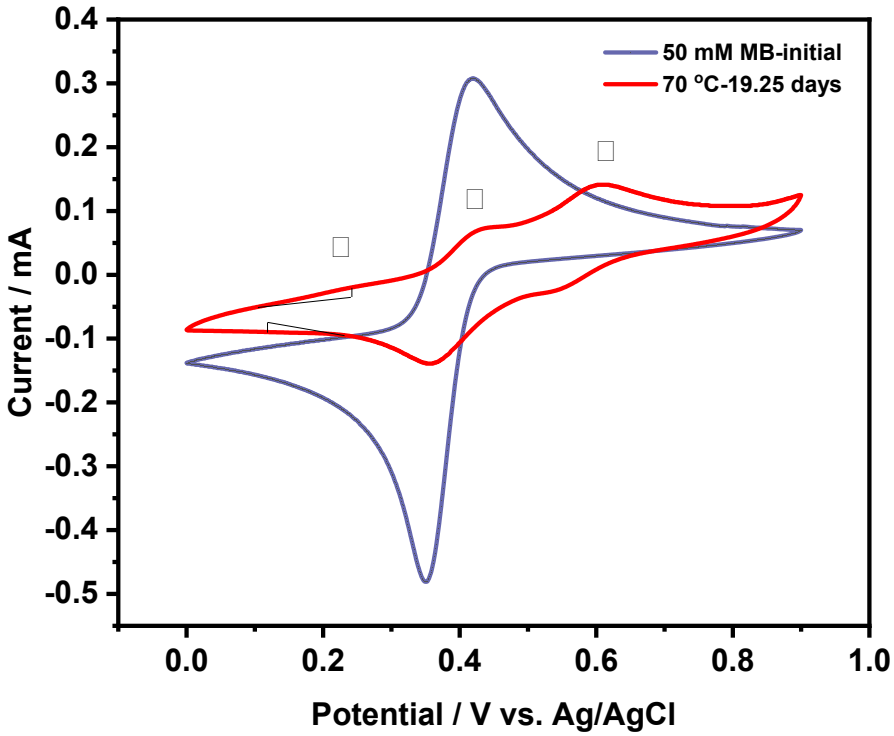

Fig. S20 CV curves of the initial 50 mM MB and stored at 70 °C for 19.25 days. There are distinct three pairs of redox peeks.

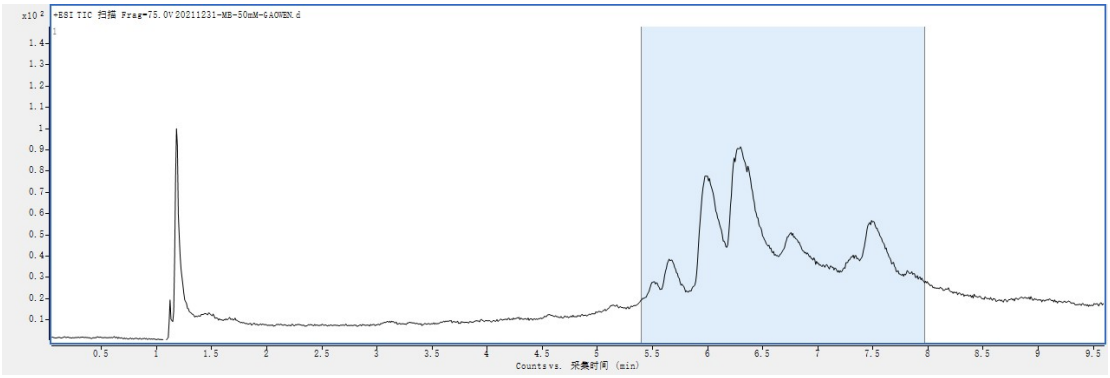

Fig. S21. A total ion chromatogram (TIC) of diluted 50 μM MB stored at 70 °C after 1 week.

References

1. Z. Yuan, Y. Duan, H. Zhang, X. Li, H. Zhang and I. Vankelecom, *Energy Environ. Sci.*, 2016, **9**, 441-447.
2. M. J. Frisch, G. W. Trucks, H. B. Schlegel, G. E. Scuseria, M. A. Robb, J. R. Cheeseman, G. Scalmani, V. Barone, G. A. Petersson, H. Nakatsuji, X. Li, M. Caricato, A. V. Marenich, J. Bloino, B. G. Janesko, R. Gomperts, B. Mennucci, H. P. Hratchian, J. V. Ortiz, A. F. Izmaylov, J. L. Sonnenberg, Williams, F. Ding, F. Lipparini, F. Egidi, J. Goings, B. Peng, A. Petrone, T. Henderson, D. Ranasinghe, V. G. Zakrzewski, J. Gao, N. Rega, G. Zheng, W. Liang, M. Hada, M. Ehara, K. Toyota, R. Fukuda, J. Hasegawa, M. Ishida, T. Nakajima, Y. Honda, O. Kitao, H. Nakai, T. Vreven, K. Throssell, J. A. Montgomery Jr., J. E. Peralta, F. Ogliaro, M. J. Bearpark, J. J. Heyd, E. N. Brothers, K. N. Kudin, V. N. Staroverov, T. A. Keith, R. Kobayashi, J. Normand, K. Raghavachari, A. P. Rendell, J. C. Burant, S. S. Iyengar, J. Tomasi, M. Cossi, J. M. Millam, M. Klene, C. Adamo, R. Cammi, J. W. Ochterski, R. L. Martin, K. Morokuma, O. Farkas, J. B. Foresman and D. J. Fox, *Journal*, 2016.
3. C. T. Lee, W. T. Yang and R. G. Parr, *Physical Review B*, 1988, **37**, 785-789.
4. S. Grimme, *Journal of Computational Chemistry*, 2004, **25**, 1463-1473.
5. S. Grimme, S. Ehrlich and L. Goerigk, *Journal of Computational Chemistry*, 2011, **32**, 1456-1465.
6. E. R. Johnson and A. D. Becke, *The Journal of Chemical Physics*, 2006, **124**, 174104.
7. P. J. Stephens, F. J. Devlin, C. F. Chabalowski and M. J. Frisch, *The Journal of Physical Chemistry*, 1994, **98**, 11623-11627.
8. Y. Zhao, N. E. Schultz and D. G. Truhlar, *Journal of Chemical Theory and Computation*, 2006, **2**, 364-382.
9. A. V. Marenich, C. J. Cramer and D. G. Truhlar, *The Journal of Physical Chemistry B*, 2009, **113**, 6378-6396.
10. F. Weigend and R. Ahlrichs, *Physical Chemistry Chemical Physics*, 2005, **7**, 3297-3305.
11. T. Lu and Q. Chen, *Computational and Theoretical Chemistry*, 2021, **1200**, 113249.
12. T. Lu and F. Chen, *Journal of Computational Chemistry*, 2012, **33**, 580-592.
13. W. Humphrey, A. Dalke and K. Schulten, *Journal of Molecular Graphics*, 1996, **14**, 33-38.
14. C. Zhang, Z. Niu, J. Bae, L. Zhang, Y. Zhao and G. Yu, *Energy & Environmental Science*, 2021, **14**, 931-939.